Article

Atomically Dispersed Copper Sites in a Metal−Organic Framework for Reduction of Nitrogen Dioxide

Yujie Ma, Xue Han, Shaojun Xu, Zi Wang, Weiyao Li, Ivan da Silva, Sarayute Chansai, Daniel Lee,* Yichao Zou, Marek Nikiel, Pascal Manuel, Alena M. Sheveleva, Floriana Tuna, Eric J. L. McInnes, Yongqiang Cheng, Svemir Rudić, Anibal J. Ramirez-Cuesta, Sarah J. Haigh, Christopher Hardacre, Martin Schröder,* and Sihai Yang*

Read Online

| ACCESS | Metrics & More | Article Recommendations | SI Supporting Information |

ABSTRACT: Metal−organic framework (MOF) materials provide an excellent platform to fabricate single-atom catalysts due to their structural diversity, intrinsic porosity, and designable functionality. However, the unambiguous identification of atomically dispersed metal sites and the elucidation of their role in catalysis are challenging due to limited methods of characterization and lack of direct structural information. Here, we report a comprehensive investigation of the structure and the role of atomically dispersed copper sites in UiO-66 for the catalytic reduction of NO_2 at ambient temperature. The atomic dispersion of copper sites on UiO-66 is confirmed by high-angle annular dark-field scanning transmission electron microscopy, electron paramagnetic resonance spectroscopy, and inelastic neutron scattering, and their location is

identified by neutron powder diffraction and solid-state nuclear magnetic resonance spectroscopy. The Cu/UiO-66 catalyst exhibits superior catalytic performance for the reduction of NO_2 at 25 °C without the use of reductants. A selectivity of 88% for the formation of N_2 at a 97% conversion of NO_2 with a lifetime of >50 h and an unprecedented turnover frequency of 6.1 h^{-1} is achieved under nonthermal plasma activation. *In situ* and *operando* infrared, solid-state NMR, and EPR spectroscopy reveal the critical role of copper sites in the adsorption and activation of NO_2 molecules, with the formation of {Cu(I)⋯NO} and {Cu⋯NO_2} adducts promoting the conversion of NO_2 to N_2. This study will inspire the further design and study of new efficient single-atom catalysts for NO_2 abatement *via* detailed unravelling of their role in catalysis.
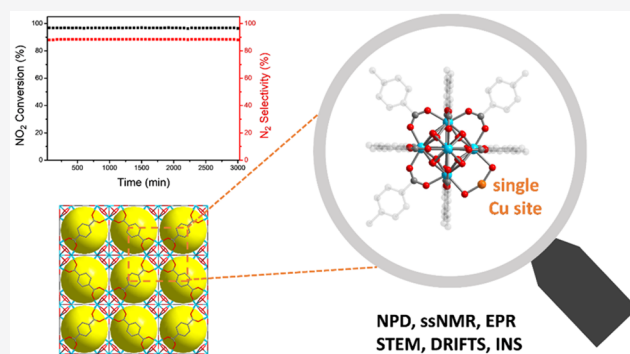
INTRODUCTION

Emerging single-atom catalysts show superior selectivity and activity in a variety of catalytic systems due to their unique electronic properties, low-coordination (or unsaturated) metal sites, and high atom efficiency.[1−4] Metal−organic framework (MOF) materials are a class of crystalline porous materials that are ideal platforms for the fabrication of single-atom catalysts due to their uniform and well-defined structure, ultrahigh porosity, and designable functionality and pore sizes.[5−8] Functional groups, such as hydroxyl bridges, and intrinsic defect sites in MOFs can enable the immobilization of atomically dispersed metal sites on the pore interior.

MOF-based single-atom catalysts have shown great promise in a number of catalytic reactions, yet the precise identification of these single-atom metal sites and their roles in catalysis remain elusive.[9−15] As a result, there is a strong motivation to develop and apply cutting-edge experimental techniques to the investigation of local structures of the single metal sites, as well as the elucidation of their roles in catalytic process, thus unravelling the catalytic pathway and mechanism. Recently, a

MOF-based single-atom catalyst, Cu/UiO-66, has been prepared by anchoring single-atom Cu sites to the defect sites of UiO-66 and used for catalytic CO oxidation and removal.[16] Herein, we conclusively identify the location of the Cu sites in Cu/UiO-66, as well as their role in the catalytic reduction of NO_2 to N_2, an important process for NO_x abatement. The local structure of structural defects and atomically dispersed Cu sites within the framework and their role in promoting the activation of substrates are elucidated by *in situ* electron paramagnetic resonance (EPR) spectroscopy, neutron powder diffraction (NPD), inelastic neutron scattering (INS), solid-state nuclear magnetic resonance (NMR) spec-
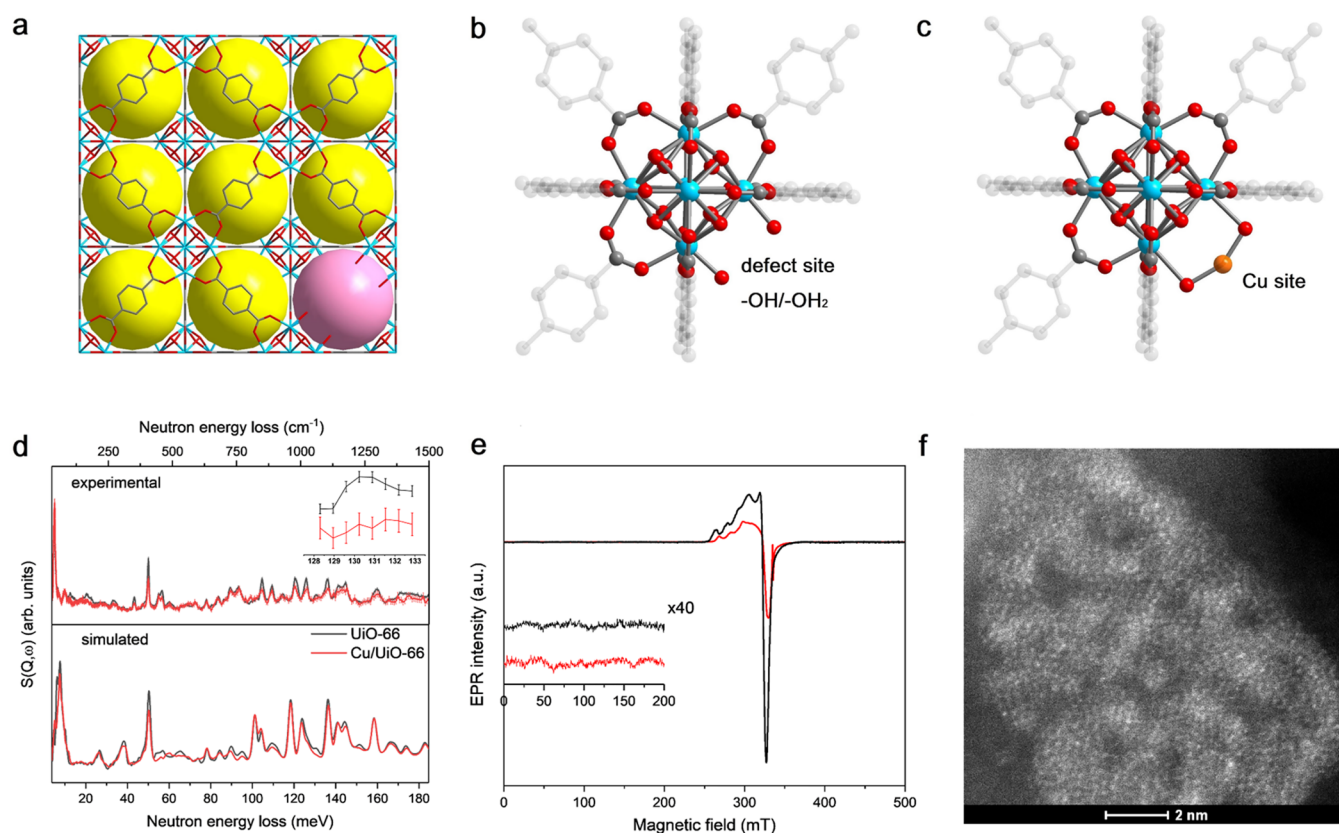
Figure 1. (a) Crystal structure of UiO-66 with a defect site. Yellow and pink spheres represent the cages without and with defect sites, respectively. (b) View of the $\{Zr_6\}$ cluster in UiO-66 with a defect site and (c) Cu/UiO-66 with a single-atom Cu site coordinated to $-OH/-OH_2$ defect sites. These structures were derived from Rietveld refinements of the NPD data at 7 K (C, gray; O, red; Zr, blue; Cu, orange; H atoms are omitted for clarity). The bond distance of Cu−O is 1.88(3) Å, and the bond angle of O−Cu−O is 152.2(1)°. (d) Comparison of the experimental and DFT calculated INS spectra of UiO-66 and Cu/UiO-66 (inset: magnification of the experimental INS features at around 130 meV). (e) X-band (9.4 GHz) EPR spectra of Cu/UiO-66 before (black) and after H_2 reduction (red), at 6.4 K (inset: expansion of low-field region confirming the absence of characteristic signals for binuclear or aggregated Cu species with $S \geq 1$). (f) HAADF-STEM image of Cu/UiO-66 after H_2 reduction.

troscopy, diffuse reflectance infrared Fourier transform spectroscopy (DRIFTS), high-angle annular dark-field scanning transmission electron microscopy (HAADF-STEM), and density functional theory (DFT) calculations. In addition to Cu/UiO-66, the catalytic performance of the −NH₂ functionalized analogue of UiO-66 (UiO-66-NH₂) has also been studied to gain insight into the potential activity of −NH₂ groups in the reduction of NO₂. Of all the catalysts studied herein, Cu/UiO-66 exhibits superior catalytic performance for the reduction of NO₂ to N₂ at room temperature without using any reducing agent under the activation of nonthermal plasma (NTP). Cu/UiO-66 shows a superior catalytic stability of >50 h in a continuous flow reaction, affording a N₂ selectivity of 88% at a 97% conversion of NO₂ with an unprecedented turnover frequency (TOF) of 6.1 h⁻¹.

RESULTS AND DISCUSSION

Synthesis and Characterization of Catalysts. UiO-66 was synthesized according to a reported method (Section S1.1).[16] UiO-66-NH₂ was prepared using the amine-functionalized ligand (2-aminoterephthalic acid) following the same procedure used for synthesizing UiO-66 (Section S1.1). Powder X-ray diffraction (PXRD) patterns (Figure S1), N₂ adsorption isotherms (Figure S2), scanning electron microscopy (SEM, Figure S3) images, and thermal gravimetric analysis (TGA, Figure S4) confirmed the successful preparation of UiO-66 and UiO-66-NH₂. The presence of structural defects (missing ligand) in desolvated UiO-66 was confirmed by NPD (Figure 1a,b), which revealed approximately one missing ligand per $\{Zr_6\}$ cluster, giving a formula of $[Zr_6O_4(OH)_4(BDC)_{5.35}(OH)_{1.30}(OH_2)_{1.30}]$ (H₂BDC ligand = benzene-1,4-dicarboxylic acid), in good agreement with previous reports.[16−18]

Cu/UiO-66 was prepared through the attachment of Cu(II) ions to the defect sites of UiO-66, followed by reduction by 5% H₂ in Ar at 250 °C for 2 h.[16] The PXRD pattern (Figure S1), N₂ adsorption isotherms (Figure S2), and SEM images (Figure S3) of Cu/UiO-66 confirm the retention of crystallinity, porosity, and crystal morphology upon the attachment of Cu to UiO-66. Elemental analysis suggested a ratio of Cu/$\{Zr_6\}$ of ~1.0, i.e., all defect sites have been filled by Cu sites.

Studies of the Atomically Dispersed Cu Sites. The location of Cu sites within Cu/UiO-66 has been determined by the Rietveld refinement of NPD data collected at 7 K (Figure 1c). Cu is coordinated to the $-OH/-OH_2$ defect sites of UiO-66 with the ratio of Cu/$\{Zr_6\}$ cluster being ~1.0. The Cu−O distance [1.88(3) Å] is in excellent agreement with that (1.89−1.95 Å) obtained from DFT calculations.[16] The binding of Cu to the $-OH/-OH_2$ defect sites was confirmed further by a combination of inelastic neutron scattering (INS) and DFT calculations (Figure 1d). Upon the binding of Cu, the INS features at 57 and 130 meV, assigned to O−H bending modes, show notable reductions in intensity, confirming the
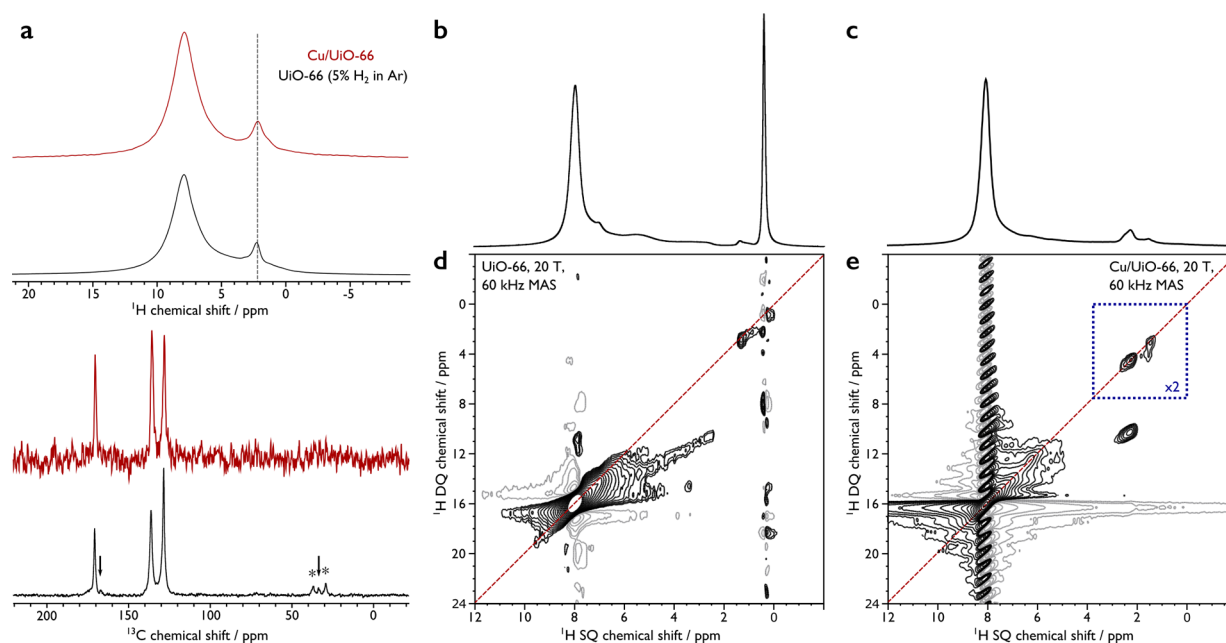
Figure 2. (a) ^{1}H DEPTH (top) and {^{1}H-}^{13}C CP (bottom) MAS NMR spectra of H_2-reduced UiO-66 (black) and Cu/UiO-66 (red). The spectra were recorded at 9.4 T using a MAS frequency of 10 kHz. The arrows and asterisks denote trace adsorbed DMF molecules and the spinning side bands, respectively. The dashed vertical gray line highlights the defect sites. ^{1}H DEPTH MAS NMR spectra of (b) UiO-66 and (c) Cu/UiO-66. 2D ^{1}H MAS NMR DQ-SQ homonuclear dipolar correlation spectra of (d) UiO-66 and (e) Cu/UiO-66, recorded using the S_3 recoupling sequence; black and gray lines represent positive and negative contours, respectively, and the dashed red line highlights the DQ diagonal. The blue square in (e) represents an area where the minimum displayed contour level has been decreased by a factor of 2 (equivalent to doubled magnification). The spectra were recorded at 20 T using a MAS frequency of 60 kHz.

coordination of Cu to these defect sites, and this was validated by DFT simulations of the INS spectra. The simulations tend to slightly underestimate the magnitude of the reduction in intensities of the small features at 100−160 meV, likely due to the overall complexity of the system. This represents the first study of the location of Cu sites within Cu/UiO-66 by diffraction techniques.

Following the determination of the location of the Cu sites, it was established that these were primarily atomically dispersed. Thus, the continuous-wave EPR spectra of Cu/UiO-66 before and after reduction under H_2 both show the characteristics of monomeric Cu(II) sites (Figure 1e).[19] No binuclear ($S = 1$) or aggregated (long-range magnetically coupled) Cu(II) species was observed by the X-band EPR spectra collected at low and room temperatures (Figure 1e and Figure S7),[20] consistent with the presence of atomically dispersed Cu(II) sites in the framework. The EPR spectra of reduced Cu/UiO-66 show that the majority of the Cu(II) sites are reduced to diamagnetic Cu(I) (Figure S8), which is consistent with X-ray photoelectron spectroscopic (XPS) analysis (Figure S17). The high-angle annular dark-field scanning transmission electron microscopy (HAADF-STEM) of Cu/UiO-66 shows many bright dots, representing Cu and Zr sites (Figure 1f and Figure S9a).[21] Although it is challenging to distinguish between Cu and Zr centers,[22] the HAADF-STEM image confirms the absence of Cu/CuO_x nanoparticles. Energy dispersive X-ray spectroscopy (EDX) mapping also shows a uniform distribution of the Cu sites (Figure S9c,d). This was further validated by the ultraviolet−visible (UV−vis) absorption spectrum of Cu/UiO-66, where the characteristic absorption peak of Cu nanoparticles [surface plasmon resonance (SPR) band] in the region of 550−600 nm[23] was not observed (Figure S10).

Analysis of Structural Defects and the Environment of Cu by Solid-State NMR. To gain further insights into the local environment of defects and Cu sites, solid-state NMR spectroscopy was employed as this has proven extremely valuable in the study of UiO-66 materials.[24,25] Here, a quantitative ^{1}H magic angle spinning (MAS) NMR spectrum of reduced UiO-66, obtained following the same treatment as Cu/UiO-66 (i.e., heating in 5% H_2 in Ar at 250 °C for 2 h), shows that this treatment removes the H center from the μ^3-OH species of the {Zr_6} cluster (Figure 2a, top), which was previously observed by variable-temperature FTIR studies.[26] ^{1}H NMR signals from low-shifted species (δ{^{1}H} < 2.5 ppm) account for ∼1/10th of the integral intensity compared to ^{1}H from the ligands (δ {^{1}H} ∼ 8 ppm) (Figure S11 and Table S3), whereas this intensity is expected to be 4 times larger for fully hydroxylated UiO-66. Therefore, these low-shifted species were assigned as −OH/−OH$_2$ centers at defect sites. The ^{1}H MAS NMR spectrum of Cu/UiO-66 (Figure 2a, top) is similar to that of reduced UiO-66, indicating that the majority of Cu(II) sites were reduced to Cu(I); a close proximity to paramagnetic Cu(II) ions would cause a substantial broadening and/or shifts of the NMR signals,[27] and this was not observed. The similarity between the ^{13}C MAS NMR spectra of reduced UiO-66 and Cu/UiO-66 (Figure 2a, bottom) demonstrates that the incorporation of Cu sites does not perturb the local ligand structure.

High-field (20 T) ^{1}H NMR spectroscopy with ultrafast MAS was also employed as this provides superior resolution. The two-dimensional (2D) double-quantum single-quantum (DQ-SQ) ^{1}H homonuclear dipolar correlation NMR spectrum (Figure 2d) for pristine UiO-66 shows the μ^3-OH species at δ {^{1}H} ∼ 0.4 ppm (Figure 2b and Figure S11). The remaining low-shifted protons at δ {^{1}H} < 2.5 ppm display both diagonal
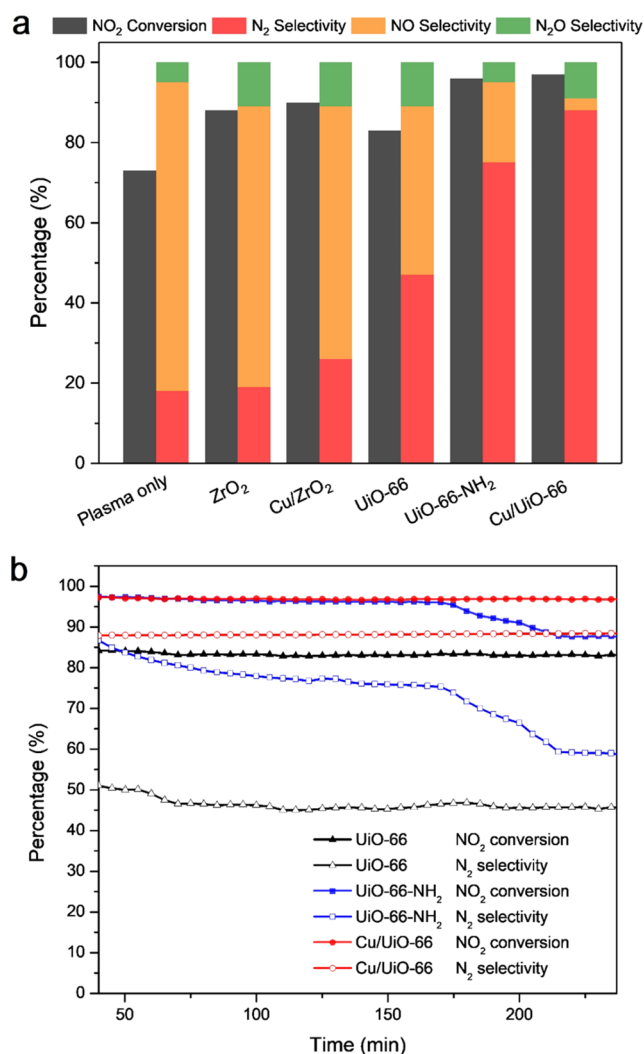
Figure 3. (a) Catalytic performance (NO_2 conversion and product selectivities) over different catalysts under steady-state NTP conditions. (b) Time-on-stream plots of NO_2 conversion and N_2 selectivity over MOF-based catalysts (UiO-66, UiO-66-NH$_2$, and Cu/UiO-66) under NTP conditions (0.4 kJ L^{-1}, 10 kHz, 500 ppm of NO_2 diluted in He, 25 °C, and atmospheric pressure).

($\delta_{SQ}\{^1H\} \sim 1.1$ ppm) will be correlated to these (off-diagonal).

The high-resolution ^1H MAS NMR spectrum of Cu/UiO-66 confirms the absence of μ^3-OH species for this sample (Figure 2c). It is also evident that there are at least three distinct defect $-OH/-OH_2$ environments at $\delta \{^1H\} \sim 2.4$, 2.2, and 1.5 ppm. The 2D DQ-SQ ^1H homonuclear dipolar correlation NMR spectrum of Cu/UiO-66 (Figure 2e) displays clear and intense autocorrelation peaks for two of the defect sites (at $\delta_{SQ} \{^1H\} \sim$ 2.4 and 2.2 ppm), indicating that they arise from OH_2 environments. Furthermore, these species also give a strong correlation with protons from the linker (at $\delta_{DQ} \{^1H\} \sim 10.3$ ppm), suggesting that they are somewhat removed from the defect site. The remaining defect proton environments are thus likely to be $-OH$ sites (at $\delta_{SQ} \{^1H\} \sim 1.5$ ppm), and cross-correlations with OH_2 environments suggest that these sites are all in close proximity and remain protonated upon the attachment of Cu sites. A quantitative comparison (Figure S11 and Table S3) between the defect sites of UiO-66 and Cu/UiO-66 suggests that displacement of adsorbed water and/or dehydroxylation of the {Zr_6} clusters during Cu attachment and subsequent H_2-reduction leads to a ~4-fold increase in the relative amount of protons at the defect sites ($\delta \{^1H\} < 2.5$ ppm). The autocorrelation peak of the lowest-shifted ^1H species of Cu/UiO-66 (at $\delta_{SQ} \{^1H\} \sim 1.5$ ppm) and its cross-correlation to OH_2 environments indicates that Cu is coordinated at defect sites as {$Zr-O(H)-Cu(OH_2)-O(H)-Zr$}. Quantitatively, this coordination mode appears approximately once every two {Zr_6} clusters. The other coordination modes of Cu sites are {$Zr-O-Cu(OH_2)-O-Zr$} and {$Zr-O-Cu-O-Zr$}. These coordination modes were confirmed by ^1H hyperfine sublevel correlation (HYSCORE) EPR spectra (Figure S12 and Table S4), which reveal a coordinated H_2O molecule in the plane perpendicular to the z axis of the electronic g matrix (the latter being perpendicular to the coordination plane) with a Cu···H distance of ~2.3 Å.

Studies of Catalytic Performance. To investigate the catalytic performance of UiO-66, UiO-66-NH$_2$, and Cu/UiO-66 for NTP-assisted decomposition of NO_2, a simulated gas flow containing 500 ppm of NO_2 diluted in helium at a total flow rate of 100 mL min^{-1} was used as the feed gas for a proof-of-concept study. Without a catalyst, the gas phase NTP alone exhibited a conversion of NO_2 (C_{NO_2}) of 73% with a low selectivity of N_2 (S_{N_2}) of 18%, with the majority of NO_2 being converted to NO, which is another major air pollutant that can be oxidized to NO_2 in air (Figure 3, Table 1, Entry 1). All three MOF catalysts can improve the C_{NO_2} and S_{N_2} (Figure 3, Table 1, Entries 2–5). UiO-66 showed a steady C_{NO_2} of 83% with a S_{N_2} of 47% over 240 min (Figure 3b).

autocorrelation peaks (between equivalent proton sites at $\delta_{DQ} \{^1H\} \sim 2.7$ ppm) and off-diagonal correlation peaks (between inequivalent proton sites at $\delta_{DQ} \{^1H\} \sim 2.4$ ppm). Accordingly, these proton environments can be assigned to defect sites (Figure 1b), where μ^1-OH_2 species ($\delta_{SQ} \{^1H\} \sim 1.3$ ppm) will give an autocorrelation peak and nearby μ^1-OH species

Table 1. Summary of the NO_2 Conversion and Product Selectivities over Different Catalysts[a]

catalyst	NO_2 conversion (%)	N_2 selectivity (%)	NO selectivity (%)	N_2O selectivity (%)
empty tube	73	18	77	5
UiO-66	83	47	42	11
UiO-66 (H_2-reduced)	85	50	40	10
UiO-66-NH$_2$	96	75	20	5
Cu/UiO-66	97	88	3	9
ZrO_2	88	19	70	11
Cu/ZrO_2	90	26	63	11

[a]Reaction conditions: 0.4 kJ L^{-1}, 10 kHz, 500 ppm of NO_2 diluted in He, 25 °C, and atmospheric pressure.
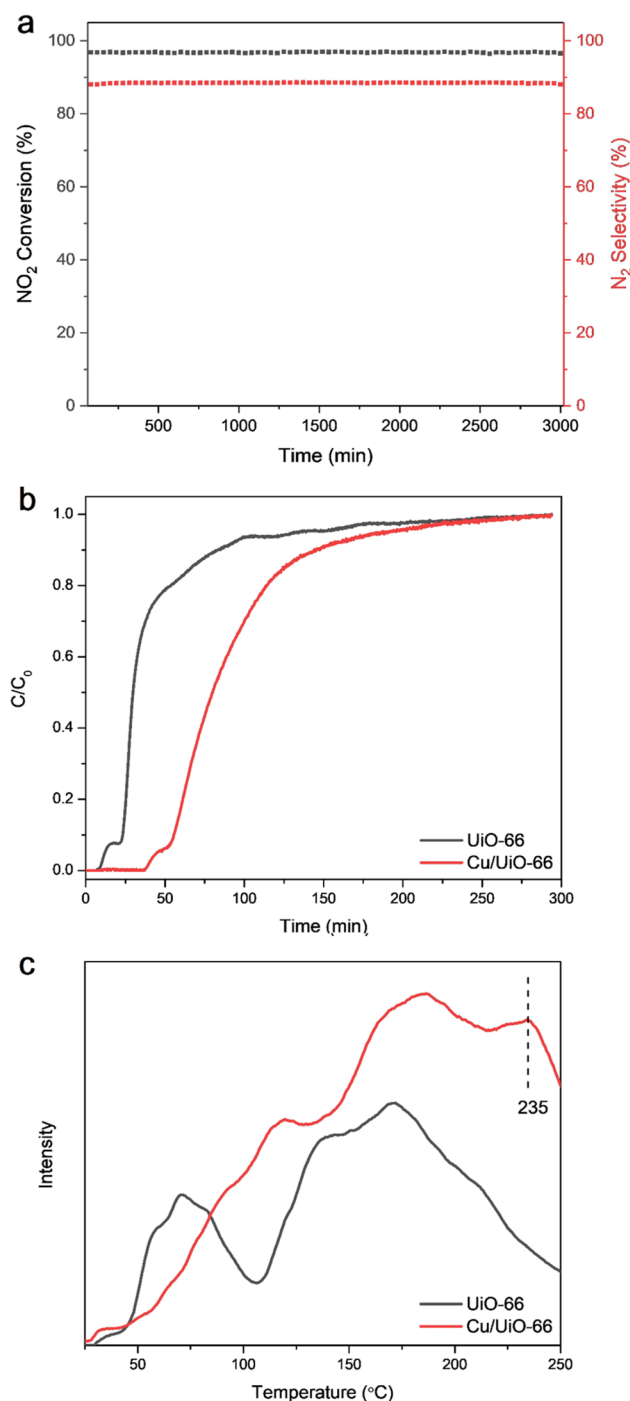
Figure 4. (a) Time-on-stream test of Cu/UiO-66 under NTP conditions. The catalytic efficiency remained constant for 50 h of reaction under continuous flow. (b) Dynamic breakthrough experiments of UiO-66 and Cu/UiO-66 using the same NO_2/He gas feed at 25 °C. (c) NO_2-TPD plots of UiO-66 and Cu/UiO-66.

The NH_2-functionalized UiO-66-NH_2 showed improvements to the catalytic activity observed for UiO-66, with the C_{NO_2} and S_{N_2} reaching 96% and 75%, respectively. However, a notable deactivation of UiO-66-NH_2 occurred after 170 min, where the C_{NO_2} and S_{N_2} dropped gradually to 88% and 59%, respectively, after 240 min (Figure 3b). The *operando* DRIFTS spectrum of UiO-66-NH_2 exposed to NO_2 under plasma activation (Figure S20) shows a new band at 2280 cm^{-1}

assigned to a diazonium salt[28] and a decrease in intensity of the bands at 3514 and 3398 cm^{-1} assigned to asymmetric and symmetric N−H stretches. These observations suggest that the −NH_2 group acts as a sacrificial agent in this reaction, with the deactivation of the catalyst being driven by the formation and dissociation of the diazonium ions upon irreversible reaction between NO_2 and the −NH_2 groups of UiO-66-NH_2. Despite the −NH_2 sites being consumed during the reaction, the overall structure of the framework in UiO-66-NH_2 was retained, as confirmed by PXRD (Figure S14).

Of the three catalysts, Cu/UiO-66 exhibits the highest catalytic efficiency, with the C_{NO_2} and S_{N_2} reaching 97% and 88%, respectively (Figure 3 and Table 1, Entry 5). Time-on-stream (ToS) tests further demonstrated the excellent catalytic stability of Cu/UiO-66 with high values for C_{NO_2} and S_{N_2} retained for over 50 h (Figure 4a). Importantly, Cu/UiO-66 exhibited a superior TOF of 6.1 h^{-1} compared with state-of-the-art Cu-based SCR catalysts, including those using NH_3 as reductant and operating at elevated temperatures (Table 2). For example, a Cu-exchanged SSZ-13 zeolite[29] shows a TOF value of 1.9−2.2 h^{-1} at 250−550 °C and Cu-MOF-74[30] demonstrates a TOF of 0.28 h^{-1} at 230 °C. Significantly, the excellent catalytic activity of Cu/UiO-66 was achieved without the use of NH_3 or heating. In contrast, Cu/ZrO_2, prepared through a similar method as for Cu/UiO-66 (Section S1.1), showed a much lower catalytic efficiency, with values of 90% and 26% for C_{NO_2} and S_{N_2}, respectively(Figure 3a and Table 1, Entry 7), indicating that the nature of atomically dispersed Cu sites within Cu/UiO-66 plays a crucial role in its observed activity. Although NTP-activated deNO$_x$ systems have been reported,[31−33] they generally suffer from poor catalytic efficiency, low TOF, and/or stability.

To explore possible sample degradation, the used Cu/UiO-66 catalyst was characterized by EPR, XPS, PXRD, DRIFTS, and N_2 adsorption isotherms. The X-band EPR spectrum of the used catalyst confirms (Figure S16) the retention of atomically dispersed Cu sites, with no evidence of aggregated species. The EPR spectrum also shows a small increase in the intensity of Cu(II) signal after reaction (Figure S8). XPS spectra indicate that the ratio of Cu(II)/Cu(I) increases after reaction, but with the majority of Cu sites still remaining as Cu(I) in the used catalyst (Figure S17). Little difference was observed in the PXRD patterns or DRIFTS spectra of fresh and used catalysts (Figures S15 and S18). N_2 adsorption isotherms at 77 K indicate a small reduction (∼10%) in the surface area of Cu/UiO-66 after reaction (Figure S19).

Studies of the Reaction Mechanism. The adsorption of NO_2 onto the catalyst is widely considered as the rate-determining step for the reduction of NO_2,[34] and dynamic breakthrough experiments were therefore carried out with UiO-66 and Cu/UiO-66 at 25 °C (Figure 4b). Notably, the dynamic adsorption capacity of NO_2 in UiO-66 increases from 2.02 to 3.96 mmol g^{-1} on incorporation of Cu sites, and the temperature-programmed desorption (TPD) profiles of NO_2-adsorbed onto UiO-66 and Cu/UiO-66 show the presence of stronger binding sites for NO_2 in the latter with an additional desorption peak at 235 °C (Figure 4c). Thus, both breakthrough and TPD experiments confirm the stronger adsorption of NO_2 in Cu/UiO-66 than in UiO-66, presumably contributing to the observed superior catalytic performance.

In situ DRIFTS spectroscopy confirmed the adsorption of NO_2, resulting in several new bands at ∼1541, 1487, 1415,

Table 2. Summary of Values of Turnover Frequency (TOF) Reported for Cu-Based Catalysts for NO$_x$ Conversion under NTP Conditions and Thermal Conditions with Reducing Agents[a]

catalyst	temperature (°C)	GHSV (10^3h^{-1})	NO$_x$ concentration (ppm)	NO$_x$ conversion (%)	TOF (h^{-1})	ToS (h)
Cu/UiO-66@NTP [this work]	25	150	500	97.0	6.1	50
HKUST-1@NTP[31]	25	75	500	97.9	0.27	0.50
Cu/ZSM-5@NTP-NH$_3$[32]	25	60	500	21.0	0.62	
Cu/ZSM-5@NTP-NH$_3$[32]	180	60	500	60.0	1.8	
Cu/MFM-300(Al)@NTP[33]	25	150	500	96	2.9	3.8
Cu-SSZ-13@thermal-NH$_3$[29]	250	30	350	95.0	2.2	
Cu-SSZ-13@thermal-NH$_3$[29]	550	30	350	83.0	1.9	
Cu-MOF-74@thermal-NH$_3$[30]	230	50	1000	97.8	0.28	24
Cu/SAPO-34@thermal-NH$_3$[46]	210	36	500	90.0	1.0	
Cu/SAPO-34@thermal-NH$_3$[46]	360	36	500	100	1.1	
Cu-ZSM-5@thermal-NH$_3$[47]	150	100	500	48.0	2.4	
Cu-ZSM-5@thermal-NH$_3$[47]	300	100	500	100	4.9	
HKUST-1@thermal-NH$_3$[48]	280	50	1000	95.5	0.26	
CuO@thermal-NH$_3$[49]	270	50	1000	97.2	0.12	25

[a]Note: GHSV = gas hourly space velocity. ToS = time-on-stream. TOF = turnover frequency.
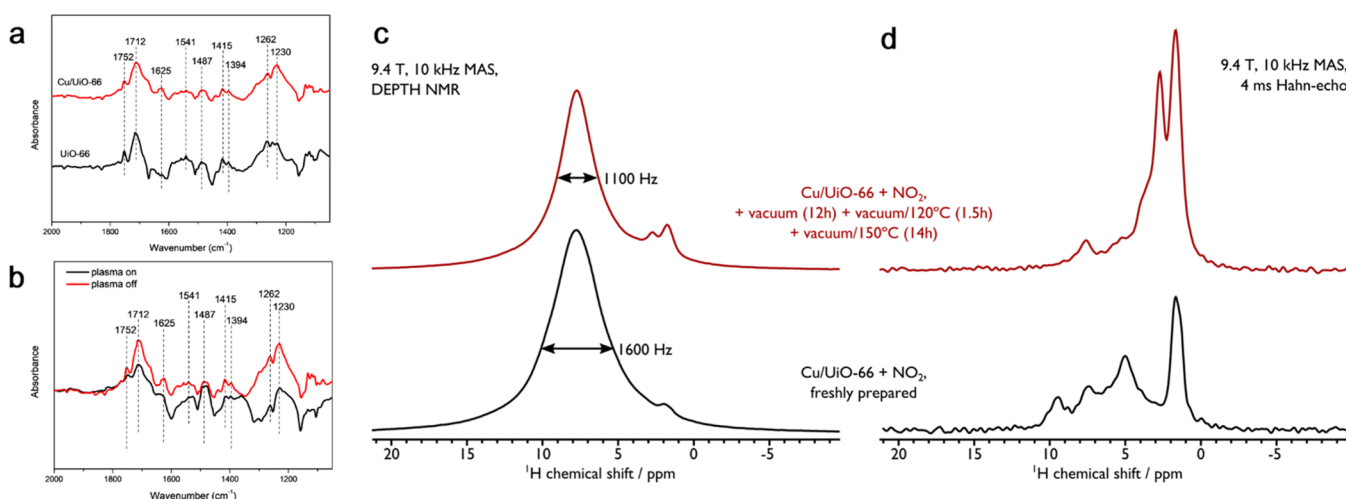
Figure 5. (a) *In situ* DRIFTS spectra of adsorbed NO$_2$ on Cu/UiO-66 (red) and UiO-66 (black). (b) *Operando* DRIFTS spectra over Cu/UiO-66 with plasma on (black) and off (red); 500 ppm of NO$_2$ in He was used as a feed gas. All the DRIFTS spectra were recorded at a resolution of 4 cm^{-1}; the spectra of bare MOF samples were subtracted as the background. (c) ^{1}H DEPTH and (d) ^{1}H-Hahn-echo MAS NMR spectra of Cu/UiO-66 dosed with NO$_2$ for 15 min (black) and the same sample after NO$_2$ desorption (red). A further desorption study can be found in the Supporting Information.

1394, 1262, and 1230 cm^{-1} (Figure 5a) assigned to various monodentate, bidentate, and bridging nitro/nitrate species[35−37] adsorbed on catalyst surfaces with partially overlapping vibrational bands. The band at 1712 cm^{-1} is associated with adsorbed NO on the −OH defect sites in both UiO-66 and Cu/UiO-66, and the notable broadening and increase of intensity of this band in Cu/UiO-66 is due to the additional contribution from the formation of {Cu(I)···NO} species.[38,39] The adsorption of NO onto the −OH defect sites was further confirmed by the depletion of the O−H stretching vibration band at 3675 cm^{-1} (Figure S21). Interestingly, an additional band was observed at 1625 cm^{-1} for NO$_2$-loaded Cu/UiO-66, which could originate from adsorbed NO$_2$ or NO species on Cu sites.[35,40,41] Thus, the formation of {Cu···NO$_2$} adducts on Cu/UiO-66 greatly accelerates the adsorption and reduction of NO$_2$. The EPR spectroscopic studies of Cu/UiO-66 and NO$_2$-loaded Cu/UiO-66 also show differences in both the *g*- and Cu hyperfine *A*-tensors (Figure S22), consistent with binding of NO$_x$ at Cu sites. *Operando* DRIFTS experiments were carried out as a function of plasma on−off and reaction time (Figure

5b). Apparent reductions of FTIR bands of various adsorbed nitro/nitrate species, {Cu(I)···NO}, and {Cu···NO$_2$} adducts were observed upon the ignition of plasma, indicating the rapid conversion of these intermediates over Cu/UiO-66. It is worth noting that, in the present system, the activation effects of NTP coupled to the adsorption of NO$_2$ by the catalyst appear to work synergistically.

In situ ^{1}H MAS NMR spectra were recorded for Cu/UiO-66 upon the adsorption of NO$_2$ to investigate the adsorbates as well as the local structural changes of the catalyst. The adsorption of NO$_2$ has substantial effects (cf. Figures 2a and 5c) with the broadening of the ^{1}H NMR signals from the ligand (at δ {^{1}H} ∼ 8 ppm) and a decrease in the intensity of signals due to the defect sites (at δ {^{1}H} < 2.5 ppm). To investigate the broadening, a ^{1}H Hahn-echo experiment[42] was employed with a relatively long total echo duration (Figure 5d) as this will remove homogeneously broadened signals [e.g., from ^{1}H centers near Cu(II) sites or with strong dipolar couplings]. Subsequently, the adsorbed NO$_2$ was removed using vacuum/heating treatment (Figure 5c and Figure S23),

which resulted in reduced line width of the ^{1}H resonance for the ligand and an increased intensity for the −OH species. Both NMR spectroscopic experiments indicate that Cu(II) is not responsible for the line broadening observed upon the adsorption of NO_2 but is a result of increased structural heterogeneity that facilitates the adsorption of NO_2 onto the MOF interior and, in addition, NO_2 binds to −OH and Cu sites, as revealed by the DRIFTS experiments. Interestingly, the increased resolution in the ^{1}H Hahn-echo MAS NMR spectrum of NO_2-adsorbed Cu/UiO-66 (Figure 5d, bottom) reveals a high-shifted ^{1}H signal at δ {^{1}H} $\sim$ 9.6 ppm, along with adsorbed bulk water at δ {^{1}H} $\sim$ 5.3 ppm; it should be noted that this experiment is not quantitative. Upon the removal of NO_2, the high-shifted ^{1}H signal and that of bulk water mostly disappear, while low-shifted −OH/OH_2 signals emerge (Figure 5d, top). The high-shifted ^{1}H signals (at δ {^{1}H} $\sim$ 9.6 ppm) can be ascribed to nitric/nitrous acid species.[43,44] The 2D ^{1}H homonuclear dipolar correlation spectrum of Cu/UiO-66 with NO_2 (Figure S24) displays correlations between these acidic protons and protons of the ligand but not with water or defect protons. Notably, this indicates that an intermediate in the reduction of NO_2 by Cu/UiO-66 could be nitric/nitrous acid and that it adsorbs, most likely through hydrogen-bonding, to the ligand. This is corroborated with data from ^{13}C MAS NMR (Figure S25), which shows a shift in the carboxylate ^{13}C signal upon adsorption of NO_2.[45]

CONCLUSIONS

The development and application of new efficient technologies to enable the precise identification of single metal sites and their roles in catalysis are important targets. We have undertaken a comprehensive study of the local structure of the single-atom Cu sites in Cu/UiO-66, thus enabling elucidation of their critical role in the reduction of NO_2. The combination of the single-atom catalyst Cu/UiO-66 and NTP leads to the direct decomposition of NO_2 to N_2 at room temperature. Cu/UiO-66 exhibits unprecedented catalytic efficiency and excellent stability. Atomically dispersed Cu sites anchored at the defect sites of the UiO-66 scaffold prevents the Cu atoms from migrating and sintering during reaction and are responsible for the superior catalytic performance. In Cu/UiO-66, the adsorption of NO_2 occurs at the Cu and hydroxyl sites, forming nitro/nitrate and related intermediates, which readily transform on activation with NTP to regenerate accessible active sites on the catalyst surface. The excellent catalytic performance of Cu/UiO-66 originates from the synergistic effects between atomically dispersed Cu sites and the framework porosity, providing multiple binding sites to promote the adsorption and conversion of NO_2. New controllable $deNO_x$ processes integrating single-atom catalysts with a NTP technique could provide an efficient solution to the mitigation of NO_x emissions.

ASSOCIATED CONTENT

Ⓢ Supporting Information

The Supporting Information is available free of charge at https://pubs.acs.org/doi/10.1021/jacs.1c03036.

Additional experimental details, PXRD and NPD data, N_2 adsorption isotherms, TGA plots, SEM and HAADF-STEM images, EPR, UV−Vis, solid-state NMR, XPS,

Auger and DRIFTS spectra, Figures S1−S25 and Tables S1−S6 (PDF)

Accession Codes

CCDC 2054313 and 2054314 contain the supplementary crystallographic data for this paper.

AUTHOR INFORMATION

Corresponding Authors

Daniel Lee − *Department of Chemical Engineering and Analytical Science, University of Manchester, Manchester M13 9PL, United Kingdom;* ⓞ orcid.org/0000-0002-1015-0980; Email: daniel.lee@manchester.ac.uk

Martin Schröder − *Department of Chemistry, University of Manchester, Manchester M13 9PL, United Kingdom;* ⓞ orcid.org/0000-0001-6992-0700; Email: M.Schroder@manchester.ac.uk

Sihai Yang − *Department of Chemistry, University of Manchester, Manchester M13 9PL, United Kingdom;* ⓞ orcid.org/0000-0002-1111-9272; Email: Sihai.Yang@manchester.ac.uk

Authors

Yujie Ma − *Department of Chemistry, University of Manchester, Manchester M13 9PL, United Kingdom*

Xue Han − *Department of Chemistry, University of Manchester, Manchester M13 9PL, United Kingdom*

Shaojun Xu − *Department of Chemistry, University of Manchester, Manchester M13 9PL, United Kingdom; UK Catalysis Hub, Research Complex at Harwell, Rutherford Appleton Laboratory, Harwell OX11 0FA, United Kingdom; School of Chemistry, Cardiff University, Cardiff CF10 3AT, United Kingdom;* ⓞ orcid.org/0000-0002-8026-8714

Zi Wang − *Department of Chemistry, University of Manchester, Manchester M13 9PL, United Kingdom*

Weiyao Li − *Department of Chemistry, University of Manchester, Manchester M13 9PL, United Kingdom*

Ivan da Silva − *ISIS Facility, STFC Rutherford Appleton Laboratory, Chilton, Oxfordshire OX11 0QX, United Kingdom;* ⓞ orcid.org/0000-0002-4472-9675

Sarayute Chansai − *Department of Chemical Engineering and Analytical Science, University of Manchester, Manchester M13 9PL, United Kingdom*

Yichao Zou − *Department of Materials, University of Manchester, Manchester M13 9PL, United Kingdom*

Marek Nikiel − *Department of Materials, University of Manchester, Manchester M13 9PL, United Kingdom*

Pascal Manuel − *ISIS Facility, STFC Rutherford Appleton Laboratory, Chilton, Oxfordshire OX11 0QX, United Kingdom*

Alena M. Sheveleva − *Department of Chemistry, University of Manchester, Manchester M13 9PL, United Kingdom; Photon Science Institute, University of Manchester, Manchester M13 9PL, United Kingdom*

Floriana Tuna − *Department of Chemistry, University of Manchester, Manchester M13 9PL, United Kingdom; Photon Science Institute, University of Manchester, Manchester M13 9PL, United Kingdom*

Eric J. L. McInnes − *Department of Chemistry, University of Manchester, Manchester M13 9PL, United Kingdom; Photon Science Institute, University of Manchester, Manchester M13 9PL, United Kingdom;* ⓞ orcid.org/0000-0002-4090-7040

Yongqiang Cheng − *Neutron Scattering Division, Neutron Sciences Directorate, Oak Ridge National Laboratory, Oak*

Ridge, Tennessee 37831, United States; ● orcid.org/0000-0002-3263-4812

Svemir Rudić − *ISIS Facility, STFC Rutherford Appleton Laboratory, Chilton, Oxfordshire OX11 0QX, United Kingdom;* ● orcid.org/0000-0003-3023-8565

Anibal J. Ramirez-Cuesta − *Neutron Scattering Division, Neutron Sciences Directorate, Oak Ridge National Laboratory, Oak Ridge, Tennessee 37831, United States*

Sarah J. Haigh − *Department of Materials, University of Manchester, Manchester M13 9PL, United Kingdom;* ● orcid.org/0000-0001-5509-6706

Christopher Hardacre − *Department of Chemical Engineering and Analytical Science, University of Manchester, Manchester M13 9PL, United Kingdom;* ● orcid.org/0000-0001-7256-6765

Complete contact information is available at:
https://pubs.acs.org/10.1021/jacs.1c03036

Notes
The authors declare no competing financial interest.

◼ REFERENCES

(1) Qiao, B.; Wang, A.; Yang, X.; Allard, L. F.; Jiang, Z.; Cui, Y.; Liu, J.; Li, J.; Zhang, T. Single-atom catalysis of CO oxidation using Pt₁/FeOₓ. *Nat. Chem.* **2011**, *3*, 634−641.

(2) Wang, A.; Li, J.; Zhang, T. Heterogeneous single-atom catalysis. *Nat. Rev. Chem.* **2018**, *2*, 65−81.

(3) Li, Z.; Ji, S.; Liu, Y.; Cao, X.; Tian, S.; Chen, Y.; Niu, Z.; Li, Y. Well-Defined Materials for Heterogeneous Catalysis: From Nanoparticles to Isolated Single-Atom Sites. *Chem. Rev.* **2020**, *120*, 623−682.

(4) Zhang, T.; Walsh, A. G.; Yu, J.; Zhang, P. Single-atom alloy catalysts: structural analysis, electronic properties and catalytic activities. *Chem. Soc. Rev.* **2021**, *50*, 569−588.

(5) Wei, Y.-S.; Zhang, M.; Zou, R.; Xu, Q. Metal−Organic Framework-Based Catalysts with Single Metal Sites. *Chem. Rev.* **2020**, *120*, 12089−12174.

(6) Bavykina, A.; Kolobov, N.; Khan, I. S.; Bau, J. A.; Ramirez, A.; Gascon, J. Metal−Organic Frameworks in Heterogeneous Catalysis: Recent Progress, New Trends, and Future Perspectives. *Chem. Rev.* **2020**, *120*, 8468−8535.

(7) Babucci, M.; Guntida, A.; Gates, B. C. Atomically Dispersed Metals on Well-Defined Supports including Zeolites and Metal−Organic Frameworks: Structure, Bonding, Reactivity, and Catalysis. *Chem. Rev.* **2020**, *120*, 11956−11985.

(8) Han, A.; Wang, B.; Kumar, A.; Qin, Y.; Jin, J.; Wang, X.; Yang, C.; Dong, B.; Jia, Y.; Liu, J.; Sun, X. Recent Advances for MOF-Derived Carbon-Supported Single-Atom Catalysts. *Small Methods* **2019**, *3*, 1800471.

(9) Zhang, E.; Wang, T.; Yu, K.; Liu, J.; Chen, W.; Li, A.; Rong, H.; Lin, R.; Ji, S.; Zheng, X.; Wang, Y.; Zheng, L.; Chen, C.; Wang, D.; Zhang, J.; Li, Y. Bismuth Single Atoms Resulting from Transformation of Metal-Organic Frameworks and Their Use as Electrocatalysts for CO₂ Reduction. *J. Am. Chem. Soc.* **2019**, *141*, 16569−16573.

(10) Ji, P.; Song, Y.; Drake, T.; Veroneau, S. S.; Lin, Z.; Pan, X.; Lin, W. Titanium(III)-Oxo Clusters in a Metal-Organic Framework Support Single-Site Co(II)-Hydride Catalysts for Arene Hydrogenation. *J. Am. Chem. Soc.* **2018**, *140*, 433−440.

(11) Li, Z.; Schweitzer, N. M.; League, A. B.; Bernales, V.; Peters, A. W.; Getsoian, A. B.; Wang, T. C.; Miller, J. T.; Vjunov, A.; Fulton, J. L.; Lercher, J. A.; Cramer, C. J.; Gagliardi, L.; Hupp, J. T.; Farha, O. K. Sintering-Resistant Single-Site Nickel Catalyst Supported by Metal−Organic Framework. *J. Am. Chem. Soc.* **2016**, *138*, 1977−1982.

(12) Zhang, Y.; Jiao, L.; Yang, W.; Xie, C.; Jiang, H.-L. Rational Fabrication of Low-Coordinate Single-Atom Ni Electrocatalysts by MOFs for Highly Selective CO₂ Reduction. *Angew. Chem., Int. Ed.* **2021**, *60*, 7607−7611.

(13) He, X.; Looker, B. G.; Dinh, K. T.; Stubbs, A. W.; Chen, T.; Meyer, R. J.; Serna, P.; Román-Leshkov, Y.; Lancaster, K. M.; Dincǎ, M. Cerium(IV) Enhances the Catalytic Oxidation Activity of Singl-Site Cu Active Sites in MOFs. *ACS Catal.* **2020**, *10*, 7820−7825.

(14) Gong, Y. N.; Jiao, L.; Qian, Y.; Pan, C. Y.; Zheng, L.; Cai, X.; Liu, B.; Yu, S. H.; Jiang, H. L. Regulating the Coordination Environment of MOF-Templated SingleAtom Nickel Electrocatalysts for Boosting CO₂ Reduction. *Angew. Chem., Int. Ed.* **2020**, *59*, 2705−2709.

(15) He, T.; Chen, S.; Ni, B.; Gong, Y.; Wu, Z.; Song, L.; Gu, L.; Hu, W.; Wang, X. Zirconium-Porphyrin-Based Metal-Organic Framework Hollow Nanotubes for Immobilization of Noble-Metal Single Atoms. *Angew. Chem., Int. Ed.* **2018**, *57*, 3493−3498.

(16) Abdel-Mageed, A. M.; Rungtaweevoranit, B.; Parlinska-Wojtan, M.; Pei, X.; Yaghi, O. M.; Behm, R. J. Highly active and stable single atom Cu catalysts supported by a metal-organic framework. *J. Am. Chem. Soc.* **2019**, *141*, 5201−5210.

(17) Trickett, C. A.; Gagnon, K. J.; Lee, S.; Gándara, F.; Bürgi, H.; Yaghi, O. M. Definitive molecular level characterization of defects in UiO-66 crystals. *Angew. Chem., Int. Ed.* **2015**, *54*, 11162−11167.

(18) Wu, H.; Chua, Y. S.; Krungleviciute, V.; Tyagi, M.; Chen, P.; Yildirim, T.; Zhou, W. Unusual and Highly Tunable Missing-Linker Defects in Zirconium Metal-Organic Framework UiO-66 and Their Important Effects on Gas Adsorption. *J. Am. Chem. Soc.* **2013**, *135*, 10525−10532.

(19) Garribba, E.; Micera, G. The determination of the geometry of Cu(II) complexes: An EPR spectroscopy experiment. *J. Chem. Educ.* **2006**, *83*, 1229−1232.

(20) Roessler, M. M.; Salvadori, E. Principles and applications of EPR spectroscopy in the chemical sciences. *Chem. Soc. Rev.* **2018**, *47*, 2534−2553.

(21) Ji, S.; Chen, Y.; Zhao, S.; Chen, W.; Shi, L.; Wang, Y.; Dong, J.; Li, Z.; Li, F.; Chen, C.; Peng, Q.; Li, J.; Wang, D.; Li, Y. Atomically

Dispersed Ruthenium Species inside Metal-Organic Frameworks: Combining the High Activity of Atomic Sites and the Molecular Sieving Effect of MOFs. *Angew. Chem., Int. Ed.* **2019**, *58*, 4271−4275.

(22) Tang, Y.; Wei, Y.; Wang, Z.; Zhang, S.; Li, Y.; Nguyen, L.; Li, Y.; Zhou, Y.; Shen, W.; Tao, F. F.; Hu, P. Synergy of Single-Atom Ni_1 and Ru_1 Sites on CeO_2 for Dry Reforming of CH_4. *J. Am. Chem. Soc.* **2019**, *141*, 7283−7293.

(23) Ben Aissa, M. A.; Tremblay, B.; Andrieux-Ledier, A.; Maisonhaute, E.; Raouafi, N.; Courty, A. Copper Nanoparticles of Well-Controlled Size and Shape: A New Advance in Synthesis and Self-Organization. *Nanoscale* **2015**, *7*, 3189−3195.

(24) Devautour-Vinot, S.; Maurin, G.; Serre, C.; Horcajada, P.; Paula da Cunha, D.; Guillerm, V.; de Souza Costa, E.; Taulelle, F.; Martineau, C. Structure and Dynamics of the Functionalized MOF Type UiO-66 (Zr): NMR and Dielectric Relaxation Spectroscopies Coupled with DFT Calculations. *Chem. Mater.* **2012**, *24*, 2168−2177.

(25) Fu, Y.; Kang, Z.; Yin, J.; Cao, W.; Tu, Y.; Wang, Q.; Kong, X. Duet of acetate and water at the defects of metal-organic frameworks. *Nano Lett.* **2019**, *19*, 1618−1624.

(26) Valenzano, L.; Civalleri, B.; Chavan, S.; Bordiga, S.; Nilsen, M. H.; Jakobsen, S.; Lillerud, K. P.; Lamberti, C. Disclosing the Complex Structure of UiO-66 Metal Organic Framework: A Synergic Combination of Experiment and Theory. *Chem. Mater.* **2011**, *23*, 1700−1718.

(27) Parigi, G.; Luchinat, C. NMR Consequences of the Nucleus−Electron Spin Interactions. In *Paramagnetism in experimental biomolecular NMR*; Luchinat, C., Parigi, G., Ravera, E., Eds.; *Royal Society of Chemistry*: London, UK, 2018; pp 1−41.

(28) Peterson, G. W.; Mahle, J. J.; DeCoste, J. B.; Gordon, W. O.; Rossin, J. A. Extraordinary NO_2 removal by the metal-organic framework UiO-66-NH_2. *Angew. Chem., Int. Ed.* **2016**, *55*, 6235−6238.

(29) Kwak, J. H.; Tonkyn, R. G.; Kim, D. H.; Szanyi, J.; Peden, C. H. Excellent Activity and Selectivity of Cu-SSZ-13 in the Selective Catalytic Reduction of NO_x with NH_3. *J. Catal.* **2010**, *275*, 187−190.

(30) Jiang, H.; Zhou, J.; Wang, C.; Li, Y.; Chen, Y.; Zhang, M. Effect of Cosolvent and Temperature on the Structures and Properties of Cu-MOF-74 in Low-temperature NH_3-SCR. *Ind. Eng. Chem. Res.* **2017**, *56*, 3542−3550.

(31) Gong, X.; Zhao, R.; Qin, J.; Wang, H.; Wang, D. Ultra-efficient Removal of NO in a MOFs-NTP Synergistic Process at Ambient Temperature. *Chem. Eng. J.* **2019**, *358*, 291−298.

(32) Wang, T.; Liu, H.; Zhang, X.; Guo, Y.; Zhang, Y.; Wang, Y.; Sun, B. A plasma-assisted catalytic system for NO removal over CuCe/ZSM-5 catalysts at ambient temperature. *Fuel Process. Technol.* **2017**, *158*, 199−205.

(33) Xu, S.; Han, X.; Ma, Y.; Duong, T. D.; Lin, L.; Gibson, E. K.; Sheveleva, A.; Chansai, S.; Walton, A.; Ngo, D.; Frogley, M. D.; Tang, C. C.; Tuna, F.; McInnes, E. J. L.; Catlow, C. R. A.; Hardacre, C.; Yang, S.; Schröder, M. Catalytic decomposition of NO_2 over a copper-decorated metal−organic framework by non-thermal plasma. *Cell Rep. Phys. Sci.* **2021**, *2*, 100349.

(34) Wikstrom, L. L.; Nobe, K. Catalytic dissociation of nitrogen dioxide. *Ind. Eng. Chem. Process Des. Dev.* **1965**, *4*, 191−195.

(35) Wang, D.; Zhang, L.; Kamasamudram, K.; Epling, W. S. In Situ-DRIFTS Study of Selective Catalytic Reduction of NO_x by NH_3 over Cu-Exchanged SAPO-34. *ACS Catal.* **2013**, *3*, 871−881.

(36) Zhang, Y.; Peng, Y.; Li, K.; Liu, S.; Chen, J.; Li, J.; Gao, F.; Peden, C. H. F. Using Transient FTIR Spectroscopy to Probe Active Sites and Reaction Intermediates for Selective Catalytic Reduction of NO on Cu/SSZ-13 Catalysts. *ACS Catal.* **2019**, *9*, 6137−6145.

(37) Sjövall, H.; Fridell, E.; Blint, R. J.; Olsson, L. Identification of adsorbed species on Cu-ZSM-5 under NH_3-SCR conditions. *Top. Catal.* **2007**, *42*, 113−117.

(38) Wright, A. M.; Sun, C.-Y.; Dincă, M. Thermal cycling of a MOF-based NO disproportionation catalyst. *J. Am. Chem. Soc.* **2021**, *143*, 681−686.

(39) Schneider, J. L.; Carrier, S. M.; Ruggiero, C. E.; Young, V. G.; Tolman, W. B. Influences of Ligand Environment on the Spectroscopic Properties and Disproportionation Reactivity of Copper-Nitrosyl Complexes. *J. Am. Chem. Soc.* **1998**, *120*, 11408−11418.

(40) Moreno-González, M.; Millán, R.; Concepción, P.; Blasco, T.; Boronat, M. Spectroscopic Evidence and Density Functional Theory (DFT) Analysis of Low-Temperature Oxidation of Cu^+ to Cu^{2+} NO_x in Cu-CHA Catalysts: Implications for the SCR-NOx Reaction Mechanism. *ACS Catal.* **2019**, *9*, 2725−2738.

(41) Kalita, A.; Kumar, P.; Mondal, B. Reaction of a copper(II)−nitrosyl complex with hydrogen peroxide: putative formation of a copper(I)−peroxynitrite intermediate. *Chem. Commun.* **2012**, *48*, 4636−4638.

(42) Hahn, E. L. Spin echoes. *Phys. Rev.* **1950**, *80*, 580−594.

(43) Steinbeck, C.; Krause, S.; Kuhn, S. NMRShiftDB - constructing a free chemical information system with open-source components. *J. Chem. Inf. Comput. Sci.* **2003**, *43*, 1733−1739.

(44) Banfi, D.; Patiny, L. Resurrecting and processing NMR spectra on-line. *Chimia* **2008**, *62*, 280−281.

(45) Bignami, G. P. M.; Davis, Z. H.; Dawson, D. M.; Morris, S. A.; Russell, S. E.; McKay, D.; Parke, R. E.; Iuga, D.; Morris, R. E.; Ashbrook, S. E. Cost-effective ^{17}O enrichment and NMR spectroscopy of mixed-metal terephthalate metal−organic frameworks. *Chem. Sci.* **2018**, *9*, 850−859.

(46) Yu, L.; Zhong, Q.; Zhang, S. Research of Copper Contained SAPO-34 Zeolite for NH_3-SCR $DeNO_x$ by Solvent-Free Synthesis with Cu-TEPA. *Microporous Mesoporous Mater.* **2016**, *234*, 303−309.

(47) Park, J. H.; Park, H. J.; Baik, J. H.; Nam, I. S.; Shin, C. H.; Lee, J. H.; Cho, B. K.; Oh, S. H. Hydrothermal Stability of Cu-ZSM-5 Catalyst in Reducing NO by NH_3 for the Urea Selective Catalytic Reduction Process. *J. Catal.* **2006**, *240*, 47−57.

(48) Jiang, H.; Wang, S.; Wang, C.; Chen, Y.; Zhang, M. Selective Catalytic Reduction of NO_x with NH_3 on Cu-BTC-derived catalysts: influence of modulation and thermal treatment. *Catal. Surv. Asia* **2018**, *22*, 95−104.

(49) Peng, B.; Feng, C.; Liu, S.; Zhang, R. Synthesis of CuO Catalyst Derived from HKUST-1 Temple for The Low-Temperature NH_3-SCR Process. *Catal. Today* **2018**, *314*, 122−128.